Article:

Yan, J. orcid.org/0009-0002-6352-7224, Zhu, Z.Q. orcid.org/0000-0001-7175-3307, Wu, X. orcid.org/0000-0002-8111-3191 et al. (3 more authors) (2025) Analysis and mitigation strategies of energy backflow in an IPMSM drive system with a small dc-link capacitor. IET Electric Power Applications, 19 (1). e70029. ISSN 1751-8660

https://doi.org/10.1049/elp2.70029

IET Electric Power Applications

ORIGINAL RESEARCH OPEN ACCESS

Analysis and Mitigation Strategies of Energy Backflow in an IPMSM Drive System With a Small DC-Link Capacitor

Jun Yan[1] | Zi Qiang Zhu[2] | Ximeng Wu[1] | Han Yang[2] | Lianghui Yang[2] | Chaohui Liu[3]

[1]Department of Electronic and Electrical Engineering, University of Sheffield, Sheffield, UK | [2]National New Energy Vehicle Technology Innovation Center (NEVC), Xiamen, China | [3]National New Energy Vehicle Technology Innovation Center (NEVC), Beijing, China

Correspondence: Zi Qiang Zhu (z.q.zhu@sheffield.ac.uk)

Received: 26 September 2024 | **Revised:** 28 February 2025 | **Accepted:** 4 April 2025

Handling Editor: Marko Hinkkanen

Funding: This work is supported by Xiamen NEVC Advanced Electric Powertrain Technology Innovation Centre, P. R. China under Agreement No. HT0502-202203010928.

Keywords: AC motor drives | current fluctuations | electrical faults | harmonics suppression | permanent magnet machines | voltage control

ABSTRACT

The energy backflow phenomenon is unavoidable in small dc-link capacitor-based PMSM drive systems, which is first identified and comprehensively analysed in this paper. This phenomenon occurs when the amplitude of the stator voltage exceeds the minimum value of the fluctuating dc-link voltage. To address this issue, flux weakening (FW) control can effectively reduce the stator voltage and mitigate the energy backflow phenomenon. However, dc-link voltage fluctuation can introduce several challenges to the conventional feedback FW control. For instance, a dc offset in the calculated d-axis reference current is identified in this paper due to the dc-link voltage fluctuation. Additionally, an analysis of the small-signal model reveals that when the fluctuating q-axis voltage becomes negative, it can lead to system instability. Moreover, the commonly used PI controller in FW control fails to adequately control the ac component introduced by these fluctuations. Therefore, this paper proposes an optimised FW control method to mitigate the energy backflow issues. Furthermore, an optimal phase angle selection method for the d-axis reference current, based on the least mean square algorithm and gradient descent algorithm, is introduced to suppress current ripple caused by the fluctuating dc-link voltage. Experimental results validate the effectiveness of the proposed optimised methods.

1 | Introduction

Permanent magnet synchronous machines (PMSMs) are widely used in various industrial and automotive applications due to their high torque density, efficiency, and robust performance [1–5]. Recently, the small dc-link capacitor-based PMSM drive systems have gained significant attention for their cost-effectiveness and compactness [6–10]. These systems are particularly popular in household appliances and applications with low control accuracy requirements [11, 12]. However, small volume dc-link capacitors can inevitably lead to the dc-link voltage fluctuation, particularly under high-speed or heavy load conditions. Such voltage fluctuations can introduce harmonic disturbances, which deteriorate the control performance and the stability of the PMSM drive systems. To better understand and address these issues, three scenarios are categorised in this paper based on different operation conditions:

1. No disturbance.
2. Considerable harmonics in the system include dc-link voltage, dc-link current, dq-axis voltages and currents and torque.
3. Energy backflow phenomenon.

The machine usually operates at low speed and light load in the first scenario. The dc-link voltage fluctuates slightly, and the harmonics in the system are negligible. Thus, there is no need for optimisation or intervention for the system.

In the second scenario, the dc-link voltage fluctuation becomes more serious with speed and/or load increases. This results in noticeable harmonics in the system. Therefore, it is necessary to optimise the control strategy and mitigate the effects of these harmonics. The predominant focus in existing research is on this second scenario. Numerous effective control strategies have been proposed to mitigate the influence of the small dc-link capacitor, leading to significant improvements in the control performance and stability of the PMSM drive system. Based on the literature review, the optimisation methods can generally be categorised into high power factor (HF) control, inductor–capacitor (LC) resonance mitigation, beat phenomenon suppression and FOC methods optimisation (flux-weakening control and sensorless control) [6, 11–14].

For the high PF control, the use of the small dc-link capacitor results in significant coupling between the grid side input power and the inverter power. This characteristic provides an opportunity to improve the grid side PF [6, 15]. The PF control method based on flux-weakening (FW) control was first proposed in ref. [16] to obtain the high PF in the small dc-link capacitor-based PMSM drive system. In ref. [17], the inverter output power is controlled directly by adjusting the reference dq-axis currents based on the current operating state of the motor and the information from dc-link voltage harmonics. Meanwhile, the grid current harmonics are suppressed by reducing the d-axis current at a low dc-link voltage area in ref. [18]. In ref. [15], an inverter power control feedback loop is implemented, where the error between actual and set power is processed through a proportional-resonant (PR) controller and applied to the q-axis reference current regulation. In refs. [19, 20], two PF correction methods for small dc-link capacitor-based PMSM drive systems are presented to achieve high PF and reduce input current harmonics. Both methods can be implemented to meet the IEC 61000-3-2 standards.

For the poor grid quality caused by LC resonance, the active damping-based mitigation methods are implemented to overcome grid current harmonics and the instability problem caused by constant power load effects [14, 21–24]. In ref. [14], the effect of virtual resistors is achieved by modifying the inverter output voltage to simulate a parallel connection with the grid side filter inductance to suppress LC resonance. Further, four configurations in which virtual resistors were either series- or parallel-connected with the grid side inductance or the dc-link capacitor is investigated in ref. [21]. Then, the configuration with virtual resistors in series with the grid side filter inductance was selected, combined with a feedforward compensation strategy, reducing the effect of grid side voltage harmonics. Furthermore, a virtual capacitor is added in parallel with the small dc-link capacitor within the drive system's topology in ref. [22]. The effect of this virtual capacitor was simulated by adjusting the reference q-axis current. However, the coupling characteristics of the d-axis power introduce some control challenges. A grid current control method is developed to improve the grid current quality by eliminating the sixth harmonics in the rectifier current in ref. [23]. In ref. [24], a grid current harmonics suppression method is proposed based on rectifier current regulation combined with the dc-link voltage decoupling method.

For the sensorless control optimisation, in refs. [25–29], different filters are developed to suppress the harmonics in estimated back-EMFs and estimated position errors to improve the accuracy of the sensorless control method.

In the third scenario, as speed and/or load increase, the dc-link voltage fluctuation becomes more serious. The amplitude of the back-EMF inevitably exceeds the fluctuating dc-link voltage during a fluctuation cycle, causing the PMSMs to act as a generator, charging the dc-link capacitor. This results in the energy backflow phenomenon. Energy backflow presents a significant challenge, especially under fluctuating voltage conditions. It occurs when the back-EMF amplitude exceeds the dc-link voltage, causing energy to flow back to the dc side. Due to the limited energy storage capacity of small electrolytic capacitors, these backflow events can cause rapid voltage rises, often leading to overvoltage conditions. Such overvoltage conditions can severely affect the motor drive's performance and safety, potentially damaging power electronic components and destabilising control. Although hardware-based solutions such as braking resistors have been proposed, they increase system complexity and cost, underscoring the need for optimised software-based control strategies to address these challenges. Existing research studies, such as the study of uncontrolled generation (UCG) operation following inverter shutdown in ref. [2] and the protection scheme for electrolytic capacitorless AC drives in ref. [30], mainly focuses on energy feedback during motor braking or inverter shutdown scenarios where the motor is not operating normally. However, in small dc-link capacitor-based PMSM drive systems, energy feedback can still occur during normal motor operation—a situation that has rarely been explored or mitigated in existing literature.

The FW control method can reduce the amplitude of the back-EMF which can relive the energy backflow phenomenon. In ref. [11], a new concept of 'average voltage constraint', combined with FW control, is proposed to mitigate the dc-link voltage fluctuation issues caused by small dc-link capacitors. In ref. [31], an enhanced FW control method is presented, which minimised torque ripple and enhanced dc-link voltage utilisation. The small-signal model of feedback FW control is implemented in ref. [32]. It is found that significant fluctuations in the q-axis voltage, especially when it turns negative, can lead the system into a positive feedback mode, resulting in inherent instability. Then, a q-axis voltage control strategy is proposed to avoid the positive feedback mode. In ref. [33], an FW control strategy based on active damping with a voltage angle adjustment method is implemented to reduce the current harmonics caused by voltage angle disturbance. In ref. [34], a systematic analysis method is proposed to evaluate the influence of transient voltage components on FW control. The inappropriate control bandwidth and insufficient voltage margin can lead to unstable operation during transient conditions. Improved design guidelines are provided to ensure stable motor control and enhanced performance. However, in PMSM drive systems with small dc-link capacitors, both the dc-link voltage and dq-axis voltages are prone to fluctuations. Conventional PI controllers of voltage loops in feedback FW control struggle to effectively manage ac harmonics. Moreover, the presence of ac components in the voltage signals can create inherent calculation errors in the d-axis reference current. This issue has not been adequately addressed in previous studies.

The fluctuating nature of the dc-link voltage introduces additional complexities to conventional FW control methods. These fluctuations induce both dc offsets and ac components in the calculated d-axis reference current, degrading control precision and exacerbating current ripple. Furthermore, when the q-axis voltage becomes negative, system instability becomes a real concern. These limitations hinder the performance of conventional FW methods. To address these challenges, this study proposes an optimised FW control method that not only mitigates energy backflow but also enhances system stability and reduces current ripple. These improvements are crucial for ensuring the reliable operation of PMSM drives, particularly in industrial and high-performance applications where precision and stability are essential.

Therefore, this paper first identifies and comprehensively analyses the energy backflow issue in the small dc-link capacitor-based IPMSM drive system. The mechanisms and possible conditions for energy backflow are then discussed in detail. The principle of energy backflow under different speed or load conditions is investigated. Furthermore, the conventional FW control method has been investigated and found to have some drawbacks due to dc-link voltage fluctuation. Therefore, a quasi-PIR-based FW control method with a dc offset compensation method is proposed to eliminate the energy backflow phenomenon. In addition, an optimal phase angle selection strategy is proposed to further reduce the harmonics and improve the control performance of the system. The analysis of the energy backflow phenomenon and the effectiveness of the proposed mitigation methods are validated by experiments.

2 | Analysis of Energy Backflow in Small DC-Link Capacitor-Based PMSM Drive System

2.1 | DC-Link Voltage Fluctuation Issues in Small DC-Link Capacitor-Based PMSM Drive System

The small dc-link capacitor-based PMSM drive system is composed of a single-phase uncontrolled rectifier, a small dc-link capacitor and an inverter as shown in Figure 1.

Due to the single-phase uncontrolled rectifier and small dc-link capacitor, the dc-link voltage can be expressed as follows:

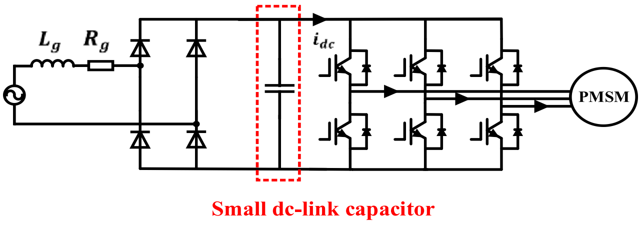

FIGURE 1 | Block diagram of PMSM drive system.

$$u_{dc} = u_{dc,0} + \sum_{k=1}^{n} u_{dc,k} \sin\left(2k\omega_g t + \varphi_{dc,k}\right) \tag{1}$$

where u_{dc} is dc-link voltage, $u_{dc,0}$, $u_{dc,k}$, and $\varphi_{dc,k}$ are the average value, the kth order harmonic, and the phase angle of fluctuating dc-link voltage, ω_g is the grid frequency.

2.2 | Principle of Energy Backflow in Small DC-Link Capacitor-Based PMSM Drive System

In the conventional PMSM drive system, a classic three-phase inverter is used to drive the PMSMs as shown in Figure 2a. Due to the small dc-link capacitor, the dc-link voltage fluctuation could cause the dc-link voltage less than the stator voltage, especially when the speed is high, and the dc-link voltage fluctuation is severe. During each dc-link voltage fluctuation cycle, when the amplitude of stator voltage is higher than the dc-link voltage, the current could flow back to the dc-link through the freewheel diodes in the inverter. The machine acts as a generator to charge the dc-link capacitor as shown in Figure 2b. Figure 3 illustrates the corresponding dq-axis equivalent circuits for the PMSMs work as the generator.

In this paper, an interior PMSM (IPMSM) is used to investigate the energy backflow. The machine voltages in the dq-axis synchronous frame are expressed by the following equation:

$$\begin{cases} u_d = R_s i_d + L_d \dfrac{di_d}{dt} - \omega_e L_q i_q \\ u_q = R_s i_q + L_q \dfrac{di_q}{dt} + \omega_e L_d i_d + \omega_e \varphi_f \end{cases} \tag{2}$$

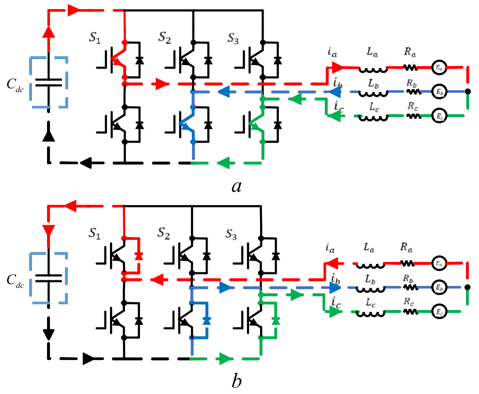

FIGURE 2 | Different operating modes. (a) Motor mode, (b) Generator mode.

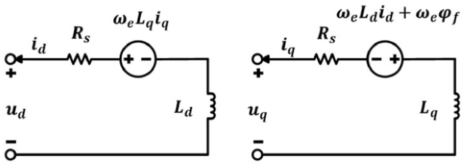

FIGURE 3 | Equivalent circuits of the IPMSM act as the generator.

where R_s, ω_e, L_d, L_q, and φ_f are the stator resistance, the motor electrical speed, the dq-axis inductances, and the flux linkage of PM, respectively.

The speed dependant stator voltage can be represented as follows:

$$u_{\text{EMF}} = \omega_e \sqrt{\left(\varphi_f + L_d i_d\right)^2 + \left(L_q i_q\right)^2} \tag{3}$$

where u_{EMF} refers to the equivalent back-EMF used in the paper to simplify the illustration. It is important to note that the equivalent back-EMF include both the voltage induced by the PM flux-linkage and the inductive voltage.

According to the amplitudes of the dc-link voltage and equivalent back-EMF, the dynamic model of three-phase uncontrolled rectifier as shown in Figure 2b can be expressed as follows:

$$\begin{cases} u_{\text{out}} = u_{\text{EMF}} - u_{\text{dc}}, & if\ u_{\text{EMF}} > u_{\text{dc}} \\ u_{\text{out}} = u_{\text{dc}} - u_{\text{EMF}}, & if\ u_{\text{EMF}} \le u_{\text{dc}} \end{cases} \tag{4}$$

where u_{out} is the voltage generated by the machine.

2.3 | Three Scenarios With Fluctuating DC-Link Voltage

Based on the relationship between the fluctuating dc-link voltage and the equivalent back-EMF, three scenarios can be classified: the equivalent back-EMF is smaller than the minimum value of dc-link voltage, the equivalent back-EMF is equal to the minimum value of dc-link voltage, and the equivalent back-EMF is greater than the minimum value of dc-link voltage. According to Equation (4), there are three operation scenarios which can be expressed by the following equation:

$$\begin{cases} u_{\text{EMF}} - u_{\text{dc,min}} < 0, & i_{\text{inv,min}} < 0 \\ u_{\text{EMF}} - u_{\text{dc,min}} = 0, & i_{\text{inv,min}} = 0 \\ u_{\text{EMF}} - u_{\text{dc,min}} > 0, & i_{\text{inv,min}} > 0 \end{cases} \tag{5}$$

where $u_{\text{dc,min}}$ and $i_{\text{inv,min}}$ are the minimum value of the dc-link voltage and the inverter current in each fluctuation cycle.

When the equivalent back-EMF is smaller than the minimum value of the dc-link voltage, there is no energy backflow. In this scenario, the harmonics in the system remain relatively small. The control performance and the system stability may not be influenced. Secondly, when the amplitude of equivalent back-EMF equals the minimum value of the fluctuating dc-link voltage, the machine continues to operate as a motor. Although there is no energy backflow, the harmonics in the system increase, with their minimum values reaching zero. The control performance and the system stability could be influenced.

The third scenario is when the amplitude of the equivalent back-EMF exceeds the minimum value of the fluctuating dc-link voltage in one dc-link voltage fluctuation cycle. In this scenario, the machine operates as a generator, resulting in a negative dc-link current and inverter output power. This negative dc-link current and inverter output power signify that the energy is being transferred from the machine back into the dc-link through the inverter. The energy backflow phenomenon is shown in Figure 4.

From A to B, the equivalent back-EMF amplitude exceeds the dc-link voltage. Starting from A, due to the energy stored in the machine inductance, the inverter power does not immediately turn negative when the equivalent back-EMF amplitude surpasses the dc-link voltage. Instead, it gradually transitions to a negative value. The inverter power becomes negative and decreases until point B, where the equivalent back-EMF equals the dc-link voltage. When the dc-link voltage becomes greater than the equivalent back-EMF amplitude from B, the inverter power gradually transitions back to positive. As the dc-link voltage rises further, the inverter power stabilises until another energy backflow phase occurs as the amplitude of the equivalent back-EMF once again approaches or exceeds the dc-link voltage from point C.

However, the energy backflow is generally considered a fault condition in low-cost drives, and this phenomenon should be avoided [11]. Furthermore, the energy backflow may lead to instability in the dc-link voltage, resulting in severe fluctuations in the system as shown in Figure 4. The peak value of dc-link voltage is maintained at 158 V, and the load torque is set to 1 Nm, whereas the motor speed is set to 800 rpm. The serious dc-link fluctuation and energy backflow in the system is a concern, as it can lead to potential operational hazards. To maintain the system stability and achieve better control performance, an effective mitigation method based on optimised FW control is proposed in the next section.

2.4 | Energy Backflow Accounting for Different Speed and Load Conditions

The increased speed can increase the amplitude of the equivalent back-EMF and slightly aggravate the dc-link voltage fluctuation. Thus, the increase in the speed might be more likely to make the PMSMs work in generation mode.

$$\omega_e \uparrow \Rightarrow \begin{matrix} \text{back} - \text{EMF} \uparrow \\ u_{\text{dc}}\ \text{fluctaution} \uparrow \end{matrix} \Rightarrow \text{Chance of energy backflow} \uparrow \tag{6}$$

With the speed increasing from 0 to a rated value, the inverter power would increase first according to the principle of power balance, if machine losses are ignored. When the speed is large enough and the equivalent back-EMF is greater than the fluctuating dc-link voltage in a certain period, the energy backflow

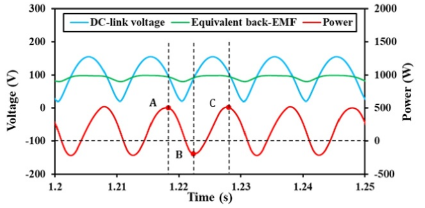

FIGURE 4 | Simulation results of energy backflow phenomenon in small dc-link capacitor-based IPMSM drive system.

occurs, and the minimum value of inverter power reduces and could be negative as shown in Figure 5a.

When the load increases from zero, the dc-link voltage fluctuation becomes larger, but the minimum value of the dc-link voltage at first is enough to keep the system stable. Thus, the minimum value of inverter power increases first. When the load further increases, the dc-link voltage fluctuation becomes severe, and the amplitude of the equivalent back-EMF may exceed the minimum value of the dc-link voltage, and the energy backflow phenomenon occurs. The minimum value of the inverter power decreases. As the load continues to increase, the average value of the dc-link current and the inverter power increases. Even if the equivalent back-EMF is greater than the dc-link voltage, the inverter power would not be negative easily due to the large stator current and the existence of inductance as shown in Figure 5b.

$$T_{\text{load}} \uparrow \Rightarrow \begin{matrix} u_{\text{dc}} \text{ fluctuation} \uparrow \\ i_{\text{dc}} \uparrow \end{matrix} \Rightarrow \text{Chance of energy backflow} \uparrow/\downarrow \tag{7}$$

The simulation results in Figure 6 show the effect of varying motor speed and load conditions on the energy backflow phenomenon. During the tests, the peak value of dc-link voltage is maintained at 158 V, the load torque is set to 1 Nm, whereas the motor speed is incrementally increased from 400 to 900 rpm, as shown in Figure 6a, the speed is set to 1000 rpm, and the load is increased from zero to 1.5 Nm.

As shown in Figure 6a, the inverter power remains positive at lower speeds, and its minimum value increases as speed rises. However, as the speed approaches a certain threshold, the amplitude of the equivalent back-EMF begins to exceed the dc-link voltage during parts of the cycle. This results in a sharp drop in the minimum inverter power, which eventually becomes negative, indicating the onset of the energy backflow phenomenon. In this condition, the motor acts as a generator, transferring energy back into the DC-link and causing a reversal of power flow.

Similarly, the system exhibits more complex behaviour under varying load conditions as shown in Figure 6b. At a constant motor speed, increasing the load initially causes the minimum value of the inverter power to rise. However, once the load exceeds a certain threshold, the dc-link voltage fluctuation becomes more serious, leading to a decline in the minimum power. Interestingly, at very high loads, the system can partially mitigate the energy backflow effect, even with a significant equivalent back-EMF exceeding the dc-link voltage. The simulation results suggest that the interplay between speed, load and dc-link voltage fluctuation plays a critical role in the occurrence and intensity of the energy backflow phenomenon.

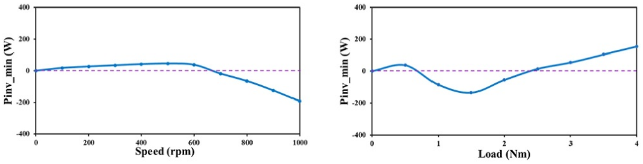

a *b*

FIGURE 5 | Energy backflow with increasing speed and load conditions. (a) With increasing speed and 1 Nm load, (b) With increasing load and 700 rpm.

Figure 7 shows the measured results of energy backflow under various operating conditions. The energy backflow issues are predominantly observed at speeds ranging from 800 to 1000 rpm, particularly when the load is between 0.5 Nm and 1.5 Nm. As can be seen, the energy backflow is most serious when the speed is 1000 rpm and the load is 1 Nm. In this case, the minimum value of the inverter power is −200 W, and the minimum value of the dc-link current is −2 A. The energy backflow could damage the power devices and deteriorate the control performance of the system. Thus, a mitigation method for the energy backflow phenomenon is critical to improve the system stability and prevent potential damage to power electronic components due to undesirable energy backflow caused by the small dc-link capacitors.

3 | Proposed Energy Backflow Mitigation Method

3.1 | Limitation of Conventional FW Control Scenarios With Fluctuating DC-Link Voltage

The FW control method can extend the speed range and maintain the performance of PMSM under low dc-link voltage conditions by reducing the amplitude of the back-EMF. Therefore, the FW control method can effectively mitigate the

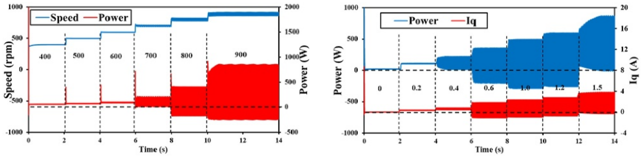

a *b*

FIGURE 6 | Simulation results of energy backflow with increasing speed and load conditions. (a) With increasing speed, (b) With increasing load.

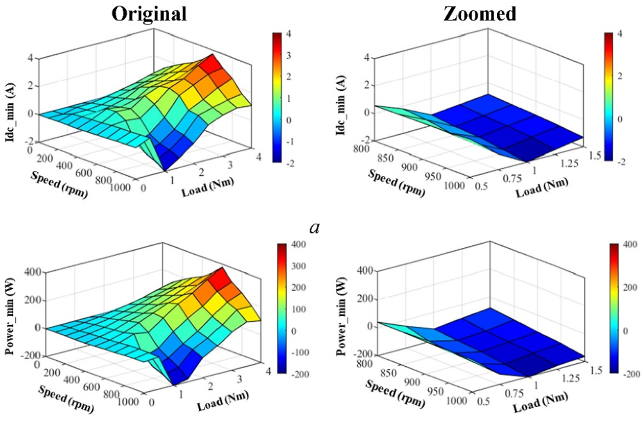

FIGURE 7 | Energy backflow accounting for different speed and load conditions. (a) Minimum value of dc-link current, (b) Minimum value of inverter power.

challenges mentioned above without introducing additional current and torque harmonics. The block diagram of the conventional feedback FW control method is shown in Figure 8. The voltage constraints ellipse can be expressed as follows:

$$u_s = \sqrt{u_d^2 + u_q^2} \leq u_{\max} = \frac{u_{\mathrm{dc}}}{\sqrt{3}} \tag{8}$$

where $u_{\max}$ is the maximum voltage that can be utilised.

If the speed is high enough and the stator resistance voltage drop is small enough, then the voltage drop by the stator resistance can be neglected. Then, Equation (8) can be approximated as follows:

$$\left(L_d i_d + \varphi_f\right)^2 + \left(L_q i_q\right)^2 \leq \frac{u_{max}^2}{\omega_e^2} \tag{9}$$

However, FW control has certain challenges in the presence of fluctuating dc-link voltage. Specifically, these voltage fluctuations induce corresponding fluctuations in the dq-axis voltages, which can degrade the control performance in the feedback FW control method. Moreover, an analysis of the small-signal model of feedback FW control in ref. [32] reveals that severe fluctuations in the q-axis voltage, particularly when it becomes negative, can cause system instability. In addition, the PI controller commonly used in conventional feedback FW control methods is unable to adequately compensate for the ac component introduced by fluctuating dc-link voltage. These challenges underline the complexity and potential instability in the application of FW control in small dc-link capacitor-based PMSM drive systems. These challenges will be explained systemically below.

3.1.1 | Saturation Issues due to Integral Operation

As shown in Figure 8, the FW control can be expressed as follows:

$$\begin{cases} u_s^* = \sqrt{u_d^2 + u_q^2} \\ i_d^* = \dfrac{K_i}{s}\left(u_{\max} - u_s^*\right) \end{cases} \tag{10}$$

where u_s^* is the amplitude of stator voltage.

Ignoring the higher-order harmonics (above 2nd order) of fluctuating dc-link voltage and dq-axis voltages, that is k equals to 1 in Equation (1), the dc-link voltage and dq-axis voltages can be expressed by the following equation [25, 29]:

$$u_{dc} = u_{dc,0} + u_{dc,1}\sin\left(2\omega_g t + \varphi_g\right) \tag{11}$$

$$\begin{cases} u_d = u_{d,0} + u_{d,1}\sin\left(\varphi_d\right) \\ u_q = u_{q,0} + u_{q,1}\sin\left(\varphi_q\right) \end{cases} \tag{12}$$

where $\varphi_d = 2\omega_g t + \varphi_{d,1}^u$, $\varphi_q = 2\omega_g t + \varphi_{q,1}^u$.

Combining Equations (10)–(12), the d-axis reference current can be expressed as follows:

$$i_d^* = \frac{K_i}{s}\left(\frac{u_{dc,0} + u_{dc,1}\sin\left(2\omega_g t + \varphi_g\right)}{\sqrt{3}} - \sqrt{\begin{array}{c} \underbrace{\left(u_{d,0}^2 + u_{q,0}^2\right)}_{\textbf{DC component}} \\ \underbrace{+2\left[u_{d,0}u_{d,1}\sin\left(\varphi_d\right) + u_{q,0}u_{q,1}\sin\left(\varphi_q\right)\right]}_{2\omega_g\ \textbf{AC component}} \\ \underbrace{+u_{d,1}^2\sin^2\left(\varphi_d\right) + u_{q,1}^2\sin^2\left(\varphi_q\right)}_{4\omega_g\ \textbf{AC component+dc offset}} \end{array}}\right) \tag{13}$$

In conventional PMSM drive systems where the dc-link voltage and dq-axis voltages have no ac harmonics, the d-axis reference current is obtained by the following equation:

$$i_d^* = \frac{K_i}{s}\left(\frac{u_{\mathrm{dc},0}}{\sqrt{3}} - \sqrt{u_{d,0}^2 + u_{q,0}^2}\right) \tag{14}$$

However, with the fluctuating dc-link voltage, the dq-axis voltages also fluctuate. As shown in Equation (13), there is a dc offset in the d-axis reference current due to the squared sinusoidal terms $u_{d,1}^2\sin^2\left(2\omega_g t + \varphi_{d,1}^u\right)$ and $u_{q,1}^2\sin^2\left(2\omega_g t + \varphi_{q,1}^u\right)$, which can be expressed as follows:

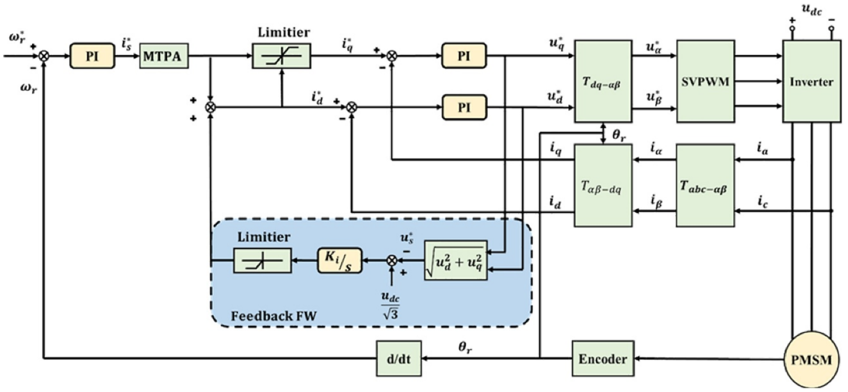

FIGURE 8 | Block diagram of the feedback FW control.

$$u_{d,1}^2 \sin^2(\varphi_d) + u_{q,1}^2 \varphi_q = u_{d,1}^2 \left(\frac{1 - \cos 2(\varphi_d)}{2} \right) + u_{q,1}^2 \left(\frac{1 - \cos 2\left(\varphi_q\right)}{2} \right) \tag{15}$$

These squared terms $u_{d,1}^2 \sin^2\left(2\omega_g t + \varphi_{d,1}^u\right)$ and $u_{q,1}^2 \sin^2\left(2\omega_g t + \varphi_{q,1}^u\right)$ have an average value of 0.5 over one period of the sinusoidal function, which introduces a dc offset in the obtained d-axis reference current. Ignoring the ac component, the d-axis reference current considering the dq-axis voltage fluctuation can be expressed as follows:

$$i_{d,e}^* = \frac{K_i}{s} \left(\sqrt{u_{d,0}^2 + u_{q,0}^2 + \frac{1}{2}\left(u_{d,1}^2 + u_{q,1}^2\right)} \right) \tag{16}$$

where $i_{d,e}^*$ represents the resulting d-axis reference current with dc-link voltage fluctuation. Hence, when the dc-link voltage and dq-axis voltage fluctuations are serious, the calculated d-axis reference current error will also become significant.

Figure 9 presents the measured results of the conventional FW control under conditions of dc-link voltage fluctuation. Due to the fluctuations in the dc-link voltage and the associated voltage calculation errors, the d-axis reference current gradually saturates. This saturation occurs because the conventional FW control does not effectively handle the voltage fluctuations, preventing proper adjustment of the d-axis current. As a result, the system is unable to maintain the desired flux weakening, and the performance of the drive system deteriorates. This failure manifests in unstable operation, as evidenced by the increasing deviation in the dc-link current and power, highlighting the limitations of the conventional FW control method in handling voltage fluctuations.

3.1.2 | Instability Issues due to Positive Feedback Mode

According to ref. [32], the small signal model of the conventional voltage feedback FW control under positive speed operating conditions is shown in Figure 10.

In Figure 10, $\frac{\partial u_s^*}{\partial i_d^*}$ is the d-axis current change on stator voltage u_s^*.

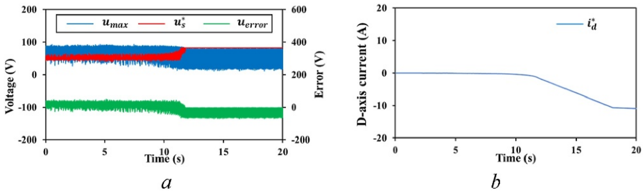

FIGURE 9 | Measured results of conventional FW control method with dc-link voltage fluctuation. (a) Voltage, (b) D-axis reference current.

$$\frac{\partial u_s^*}{\partial i_d^*} = \frac{\partial u_s^*}{\partial u_d^*} \frac{\partial u_d^*}{\partial i_d^*} + \frac{\partial u_s^*}{\partial u_q^*} \frac{\partial u_q^*}{\partial i_d^*} \tag{17}$$

According to Equations (2) and (9)

$$\frac{\partial u_s^*}{\partial i_d^*} = \frac{u_d R_s + u_q \omega_r L_d}{\sqrt{u_d^2 + u_q^2}} \tag{18}$$

Therefore, when $\frac{\partial u_s^*}{\partial i_d^*} > 0$, u_s^* is the increasing function of i_d^* and the closed-loop system is negative feedback, the system is stable. However, when $\frac{\partial u_s^*}{\partial i_d^*} < 0$, u_s^* is the decreasing function of i_d^* and the closed-loop system is positive feedback, which is unstable. Therefore, the stable conditions should be,

$$u_d R_s + u_q \omega_r L_d > 0 \tag{19}$$

In high-speed operation, the above equation can be simplified as $u_q > 0$; if $u_q < 0$, the system would be unstable as shown in Figure 11.

In small dc-link capacitor-based PMSM drive systems, the u_q can become negative due to the combined effects of energy backflow and voltage fluctuations. During the energy backflow phenomenon, the negative i_q current component, combined with the dynamic effects of current-derivative terms $\left(di_q/dt\right)$, leads to a rapid drop in the q-axis voltage u_q. As a result, u_q may fall below zero even before the d-axis current i_d reaches its conventional FW threshold of $-\varphi_f/L_d$. This situation is further exacerbated by the fluctuating nature of the dc-link voltage and the dq-axis voltages, which introduce significant oscillations into the reference i_d current. As the system operates in deep FW regions, these fluctuations cause i_d to vary around the threshold, resulting in transient conditions where $i_d < -\varphi_f/L_d$; thus, u_q becomes negative. This negative u_q reflects the combined effect of equivalent back-EMF dynamics, rapid voltage changes, and control system response to fluctuating power conditions.

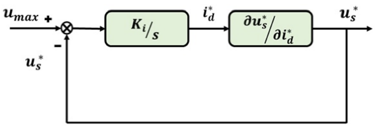

FIGURE 10 | Small signal model of feedback FW control method.

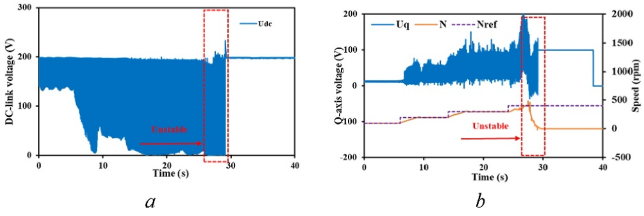

FIGURE 11 | Unstable issues with negative q-axis voltage. (a) DC-link voltage, (b) Q-axis voltage and speed.

3.2 | Proposed Optimised FW Control

Figure 12 shows the block diagram of the proposed optimised FW control method. In the proposed method, a quasi-PIR controller is employed to control the harmonic components of the voltage error. The resonant gain K_r is set to 1, and the integral frequency ω_i is set to 5 rad/s, respectively. Unlike the conventional PI controller, which is typically effective for steady-state error correction but may fall short in addressing periodic disturbances, the quasi-PIR controller integrates a resonant component that is fine-tuned to the frequency of the system harmonics. Compared with the traditional PIR controller, the quasi-PIR controller is designed to provide better control performance in scenarios where disturbances are not strictly limited to a single frequency [35]. The transfer function of the quasi-PIR controller is presented by the following equation:

$$G_{\mathrm{PIR}}(s) = K_p + \frac{K_i}{s} + \frac{2\omega_i K_r s}{s^2 + 2\omega_i s + \omega_g^2} \tag{20}$$

The bode diagram of the quasi-PIR is shown in Figure 12.

Figure 13 shows the whole block diagram of the optimised FW control strategy. Firstly, the dc offset is compensated for voltage calculation errors caused by voltages fluctuation. Secondly, a signal processing procedure is utilised to obtain the amplitude of the ac components of the dq-axis voltages as shown in Figure 14. In addition, a q-axis voltage limiter is employed to prevent the q-axis voltage from becoming negative.

3.3 | Optimal Phase Angle Selection of D-Axis Reference Current

Because the d-axis reference current contains the ac component, it is essential to consider the phase angle. As optimal current angle selection enables achieving maximum output torque with minimal current, thus ensuring optimal control performance. By precisely adjusting the phase angle, the fluctuations in the system can be suppressed. The performance of the system can be improved. The d-axis reference current can be expressed by the following equation:

$$i^{\mathrm{ref}}_{\mathrm{d},2\omega_{\mathrm{g}}} = i^{\mathrm{ref}}_{\mathrm{d,dc}} + i^{\mathrm{ref}}_{\mathrm{d,ac},2\omega_{\mathrm{g}}} \cos\left(2\omega_g t + \varphi_{\mathrm{i}_{\mathrm{d,ac},2\omega_{\mathrm{g}}}}\right) \tag{21}$$

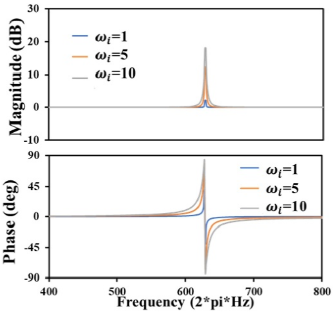

FIGURE 12 | Bode diagram of the quasi-PIR controller.

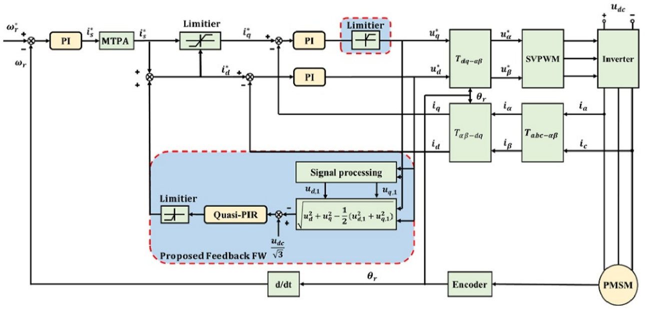

FIGURE 13 | Block diagram of optimised FW method.

where $i^{\mathrm{ref}}_{\mathrm{d},2\omega_{\mathrm{g}}}$ is the d-axis reference current, $i^{\mathrm{ref}}_{\mathrm{d,dc}}$ is the amplitude of the dc component of d-axis reference current, $i^{\mathrm{ref}}_{\mathrm{d,ac},2\omega_{\mathrm{g}}}$, and $\varphi_{\mathrm{i}_{\mathrm{d,ac},2\omega_{\mathrm{g}}}}$ are the amplitude and phase of the 2nd order harmonic of d-axis reference current. The signal demodulation method shown in Figure 14 is used to extract the phase information of the ac component of the injected d-axis current. The bandwidth of the PI regulator in the signal demodulation process is set relatively low (1/5 to 1/10 of the current controller bandwidth) to ensure system stability without compromising dynamic response. This tuning approach facilitates smooth angle estimation while maintaining fast dynamic performance in other control loops, thereby ensuring both accuracy and desired dynamics through trial-and-error adjustments. This phase information is crucial for optimising the control of the injected current using the gradient descent (GD) algorithm [36].

Due to the presence of an ac component in the injected d-axis current, the phase of the d-axis reference current becomes crucial for system performance. By adjusting the phase angle of the d-axis reference current, the relative alignment between the magnetic field and the rotor can be optimised, directly influencing the motor's efficiency and torque generation. Proper phase alignment ensures optimal magnetic field interaction, reducing losses and enhancing torque production. As a result, optimising the phase of the injected d-axis current helps to mitigate q-axis current pulsation caused by dc-link voltage fluctuations.

Based on this relationship, the GD algorithm is employed to determine the optimal phase angle of the d-axis reference current. By using the GD algorithm, the optimal phase angle can be selected by minimising the q-axis current harmonics at twice the grid frequency.

This paper uses the GD algorithms to improve the accuracy and robustness of the optimal phase angle selection. The structure of the optimal phase angle selection is shown in Figure 15. The 100 Hz ac component of q-axis current $i_{\mathrm{q,ac},2\omega_{\mathrm{g}}}(n)$ is the input signal. The phase angle of d-axis reference current $\varphi_{\mathrm{i}_{\mathrm{d,ac},2\omega_{\mathrm{g}}}}(n)$ is considered as the weight factor.

The output signal O_n is presented by the following equation:

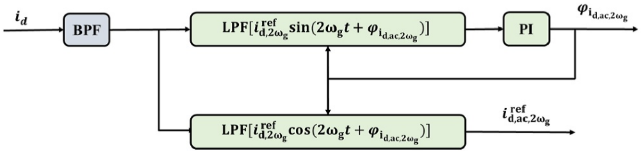

FIGURE 14 | Block diagram of signal demodulation method.

$$O_n = i_{\mathrm{q,ac},2\omega_{\mathrm{g}}}(n) \times \varphi_{i_{\mathrm{d,ac},2\omega_{\mathrm{g}}}}(n) \tag{22}$$

where $i_{\mathrm{q,ac},2\omega_{\mathrm{g}}}(n)$ is the 100 Hz ac component of q-axis current.

The output signal O_n of the GD algorithm is the product of the 100 Hz ac component of the q-axis current $i_{\mathrm{q,ac},2\omega_{\mathrm{g}}}(n)$ and the phase angle of the injected d-axis reference current $\varphi_{i_{\mathrm{d,ac},2\omega_{\mathrm{g}}}}(n)$. This product represents the interaction between the q-axis current ripple and the phase angle of the d-axis reference current, which can be adjusted to minimise the q-axis current ripple.

The error $\mathrm{Err_n}$ between the desired response D_n and the output signal O_n can be expressed as follows:

$$\mathrm{Err}_n = D_n - O_n = 0 - i_{\mathrm{q,ac},2\omega_{\mathrm{g}}}(n) \times \varphi_{i_{\mathrm{d,ac},2\omega_{\mathrm{g}}}}(n) \tag{23}$$

where the desired response D_n is set to zero, indicating the goal of eliminating the 100 Hz AC component in the q-axis current.

The objective function J_n can be defined as half of the squared error criterion as expressed by the following equation:

$$J_n = 0.5(\mathrm{Err}_n)^2 = 0.5\left[-i_{\mathrm{q,ac},2\omega_{\mathrm{g}}}(n) \times \varphi_{i_{\mathrm{d,ac},2\omega_{\mathrm{g}}}}(n)\right]^2 \tag{24}$$

The above objective function J_n, which represents the squared error between the desired and actual system outputs, is minimised to optimise the performance. The purpose of this objective function is to find the optimal phase angle of the d-axis reference current $\varphi_{i_{\mathrm{d,ac},2\omega_{\mathrm{g}}}}(n)$ that minimises Err_n, thereby eliminate the q-axis current ripple $i_{\mathrm{q,ac},2\omega_{\mathrm{g}}}(n)$.

The optimal phase angle $\varphi^{\mathrm{inj}}_{i_{\mathrm{d,ac},2\omega_{\mathrm{g}}}}$ can be trained by the GD algorithm to minimise the objective function as presented by the following:

$$\varphi_{i_{\mathrm{d,ac},2\omega_{\mathrm{g}}}}(n+1) = \varphi_{i_{\mathrm{d,ac},2\omega_{\mathrm{g}}}}(n) + \xi\left[-\nabla J_{(n)}\right] \tag{25}$$

where $\nabla J_{(\mathrm{n})}$ represents the gradient, ξ stands for the constant training, determining the convergence speed.

The flow chart of the GD algorithm is shown in Figure 16.

The weight factors are updated in the opposite direction of the gradient $\nabla J_{(\mathrm{n})}$ as the goal is to minimise the 100 Hz q-axis current harmonics. Consequently, $\varphi_{i_{\mathrm{d,ac},2\omega_{\mathrm{g}}}}(n)$ can be trained to an optimised value.

If $i_{\mathrm{q,ac},2\omega_{\mathrm{g}}}(n) > i_{\mathrm{q,ac},2\omega_{\mathrm{g}}}(n\ +\ 1)$, the descent direction is right; If $i_{\mathrm{q,ac},2\omega_{\mathrm{g}}}(n) < i_{\mathrm{q,ac},2\omega_{\mathrm{g}}}(n\ +\ 1)$, the descent direction is wrong.

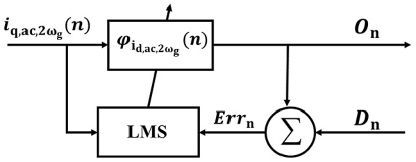

FIGURE 15 | Block diagram of GD algorithm.

Then, the optimal phase angle can be obtained by minimising the q-axis current harmonics. The block diagram of the proposed energy backflow mitigation method, together with the optimal phase angle selection method, is shown in Figure 17.

4 | Experimental Validation

In this section, the analysis of the energy backflow issue is verified, and the effectiveness of the proposed mitigation methods are demonstrated. The experimental platform is designed using a variable transformer and an isolation transformer connected to the main power, providing an adjustable and isolated ac input source. The platform is built around the Infineon EVAL-M1-CTE610N3 evaluation board, which is used to control and interface with the system. The dSPACE1006 control system is employed to manage the operations. The platform includes both a test motor (IPMSM) and a load machine (dc machine), as shown in Figure 18. The ac power supply with a 158 V peak value is used. The specifications of the system are given in Table 1.

4.1 | Simulation Results of the Proposed Method

Figure 19 shows the simulation results of the small dc-link capacitor-based IPMSM drive system, with and without the proposed method. The operation conditions are the same as those in Figure 4.

Before 0.5 s, without the proposed method, considerable harmonic distortion is observed in the voltages, currents, and

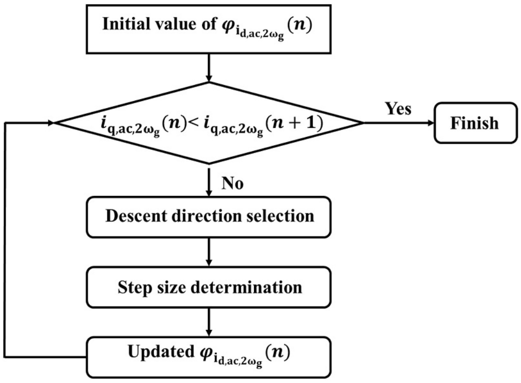

FIGURE 16 | Flow chart of GD algorithm.

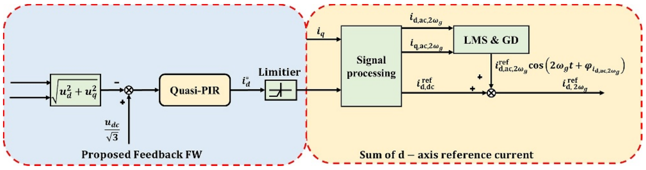

FIGURE 17 | Block diagram of proposed energy backflow suppression method with optimal phase angle selection method.

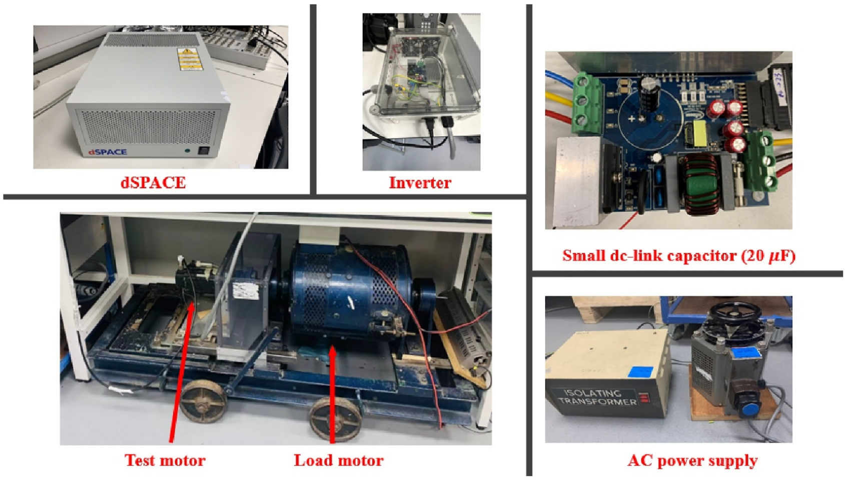

FIGURE 18 | Experimental platform.

TABLE 1 | Machine parameters.

Parameter	Value	Parameter	Value
Rated voltage	158 V	Rated current	4 A
Rated power	0.6 kW	Rated torque	4 Nm
Switching frequency	10 kHz	Flux-linkage	0.2505 Wb
Rated speed	1000 rpm	Pole pairs	3
DC-link capacitance	20 μF	Stator resistance	6 Ω
D-axis inductance	40 mH	Q-axis inductance	60 mH

torque, particularly at 100 Hz. The peak-to-peak value of the fluctuating dc-link voltage is approximately 128 V, whereas the peak-to-peak power variation reaches around 230 W. Torque fluctuations are approximately 2.2 Nm. Additionally, energy backflow occurs as the back-EMF exceeds the minimum value of the fluctuating dc-link voltage. These oscillations, resulting from harmonic interactions and energy backflow, degrade system stability, and increase current harmonic distortion.

After 0.5 s, these fluctuations are greatly mitigated with the proposed method. The peak-to-peak value of the dc-link voltage decreases from 128 to 85 V, and the peak-to-peak power variation is reduced from 230 to 105 W. Torque fluctuations are also reduced from 2.2 Nm to 1.2 Nm. Furthermore, the fluctuating dc-link voltage is effectively suppressed, and the minimum value of the fluctuating dc-link voltage exceeds the back-EMF. These improvements stabilise the system, effectively eliminating the energy backflow phenomenon. The simulation results demonstrate the efficacy of the proposed method in reducing harmonic distortion, eliminating energy backflow and enhancing system stability.

4.2 | Proposed Optimised FW Control

Figure 20 shows the measured results without and with the optimised FW method under three different operating conditions: (from left to right) 800 rpm with a 0.5 Nm load, 800 rpm with a 1 Nm load and 1000 rpm with a 0.5 Nm load.

At the first condition (800 rpm with 0.5 Nm load), without the optimised FW method, the equivalent back-EMF exceeds the minimum value of the dc-link voltage before 5 s, leading to the energy backflow phenomenon. This is evident from fluctuations in the dc-link current, torque and inverter power, which exhibit both positive and negative values. The maximum backflow q-axis current reaches approximately 0.35 A, and the backflow power approaches 50 W. Consequently, the dc-link cannot handle the backflow energy, causing an increase in the dc-link voltage amplitude from 160 to 170 V. After applying the optimised FW method at 5 s, the negative dc-link current, torque and inverter power are significantly reduced, effectively suppressing the energy backflow. When the load is increased to 1 Nm (middle column), the energy backflow phenomenon becomes more pronounced without the FW method. However, after 5 s, the optimised FW method is applied and the energy backflow is effectively suppressed, with the dc-link current and inverter power returning to stable positive values.

At the final condition (1000 rpm with 0.5 Nm load, right column), the equivalent back-EMF exceeds the dc-link voltage again before 5 s, causing energy backflow. After 5 s, the backflow is eliminated when the optimised FW method is activated. In summary, Figure 20 demonstrates the effectiveness of the optimised FW method in mitigating energy backflow under various conditions, reducing system instability, and improving the overall performance of the PMSM drive system. The optimised FW method not only suppresses negative current and power but also reduces current harmonics, contributing to enhanced system reliability across various operating scenarios.

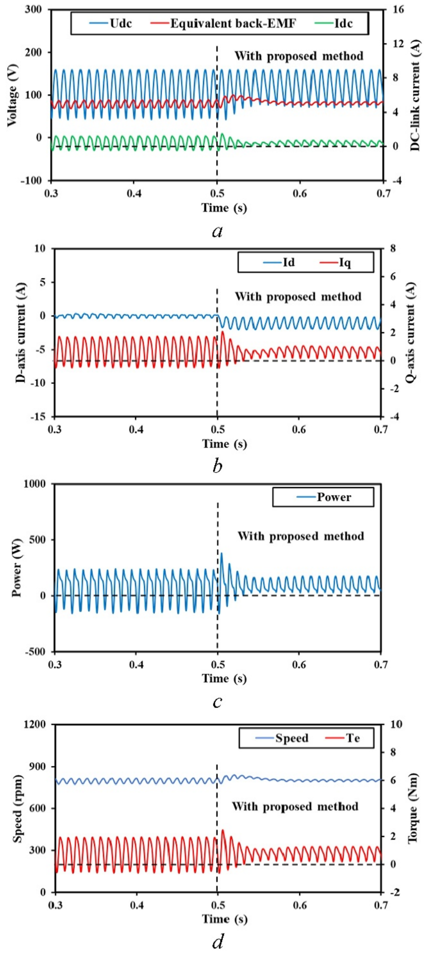

FIGURE 19 | Simulation results without and with the proposed method. (a) DC-link voltage, equivalent back-EMF, and dc-link current, (b) dq-axis current, (c) Power, (d) Speed and torque.

Figure 21 shows the summary of the proposed optimised FW method in eliminating the energy backflow phenomenon under different operating conditions. By the proposed method, the maximum backflow current is reduced from −2 to 0 A, and the maximum backflow power is from −200 to 0 W.

4.3 | Optimal Phase Angle Selection of D-Axis Reference Current

Figure 22 shows the measured results both without and with the optimal phase angle selection method under three different operating conditions: (from left to right) 800 rpm with a 0.5 Nm load, 800 rpm with a 1 Nm load, and 1000 rpm with a 0.5 Nm load. At the first condition (800 rpm with a 0.5 Nm load, left column), the system operates with the d-axis reference current without the optimal phase angle selection method before 4 s, which results in an obvious 100 Hz harmonic in the system due to the dc-link voltage fluctuation. This harmonic appears prominently in the current waveforms, causing a ripple in the system. After 4 s, when the d-axis reference current is reconstructed by the optimal phase angle selection method, a significant reduction in the 100 Hz harmonic is observed, with the harmonic amplitude of the q-axis current decreasing from 0.25 to 0.12 A.

When the load is increased to 1 Nm (middle column), the 100 Hz harmonic in the q-axis current is noticeably reduced from 0.5 to 0.3 A after the d-axis reference current reconstruction. This reduction confirms that the optimal phase angle selection method can effectively suppress harmonics in the system, even under higher load conditions.

At the final condition (1000 rpm with 0.5 Nm load, right column), the system shows a similar trend. Before 4 s, the 100 Hz harmonic in the q-axis current is present, reaching a value of 0.38 A. After 4 s, the optimal phase angle selection method is applied, significantly reducing the harmonic amplitude to 0.15 A. These results clearly show that the 100 Hz harmonic is effectively reduced by optimising the phase angle of the d-axis reference current.

Figure 22 demonstrates that the proposed optimal phase angle selection method enhances the performance of the system by reducing current harmonics under various operating conditions. This method improves system stability, particularly when dealing with the challenges introduced by small dc-link capacitors and proves effective with varying load conditions.

Table 2 presents a comparison of simulation and experimental results for the conventional FW method under three operating conditions: 800 rpm with a 0.5 Nm load, 800 rpm with a 1 Nm load and 1000 rpm with a 0.5 Nm load. The comparison includes the harmonic amplitudes of the dc-link voltage, dq-axis currents and power. However, the conventional method struggles to suppress the 100 Hz harmonic component in the system, resulting in a noticeable harmonic distortion.

Table 3 highlights the performance of the proposed method under identical operating conditions. The results demonstrate that the simulation results are closely aligned with the experimental trends. Additionally, the proposed methods improve the harmonic suppression, particularly for the 100 Hz component. This improvement validates the effectiveness of the proposed methods in reducing dc-link voltage fluctuations and enhancing system performance.

Figures 23 and 24 show the spectra of the q-axis current without and with the proposed optimal phase angle selection method under different operation conditions. These measured results illustrate that the control performance of the system is improved under various speed and load conditions by selecting the optimal d-axis reference current phase angle.

Figures 25 and 26 show the dynamic performance of the proposed methods under different operating conditions.

In Figure 25, the speed is increased from 600 to 700 rpm with a constant load of 0.5 Nm. In the left column, where the proposed method is not applied, significant fluctuations in the dc-link voltage are observed during the speed ramp-up. These fluctuations cause the equivalent back-EMF to exceed the dc-link voltage, leading to the energy backflow phenomenon. As a result, the dc-link current reaches a negative peak of nearly 2 A, with the maximum negative power approaching 200 W and the maximum negative torque near 2.5 Nm. The right column shows the results when the proposed method is applied. The

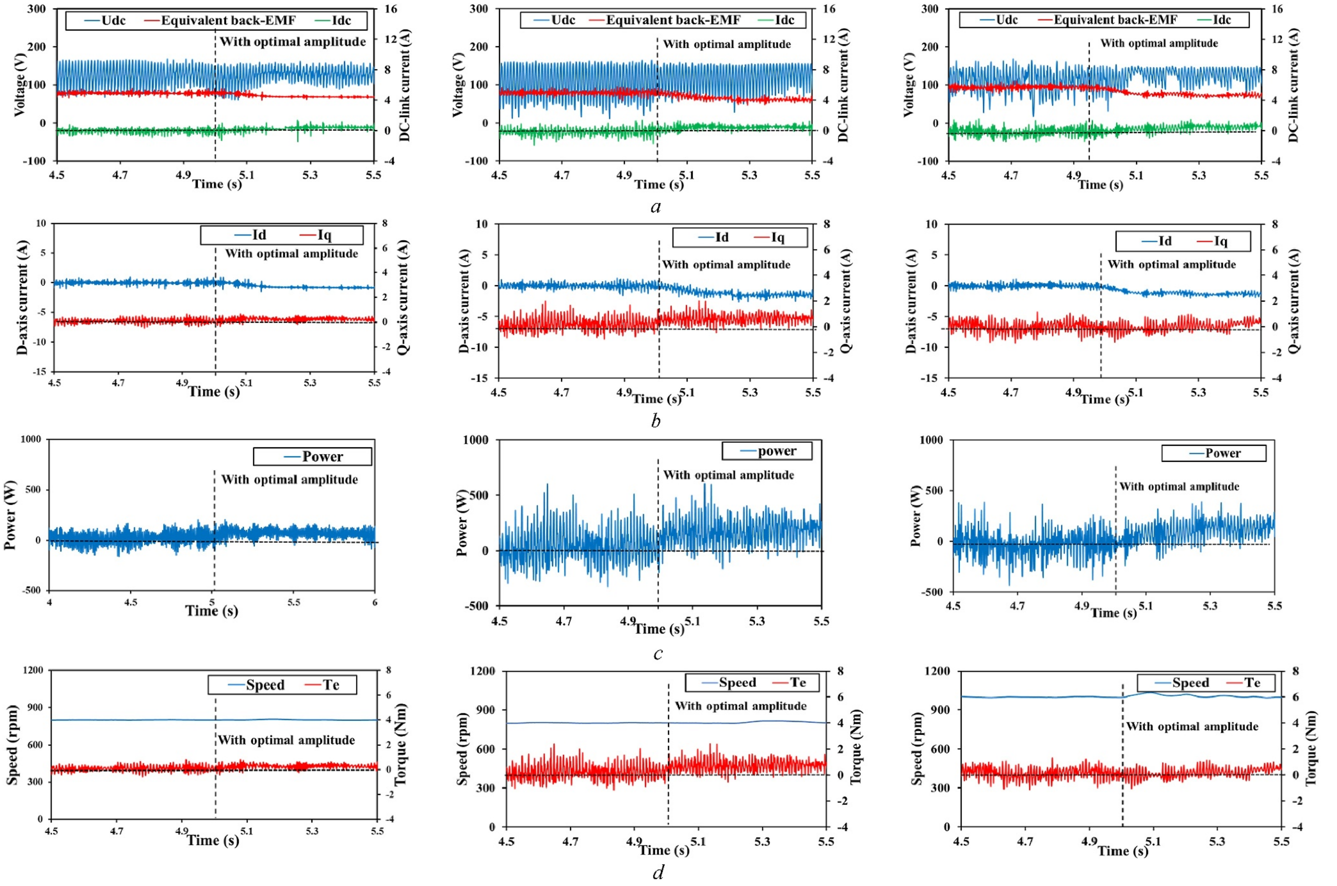

FIGURE 20 | Measured results without and with the proposed optimised FW method (from left to right, 800 rpm with 0.5 Nm load, 800 rpm with 1 Nm load, 1000 rpm with 0.5 Nm load). (a) DC-link voltage, equivalent back-EMF, and dc-link current, (b) dq-axis current, (c) power, (d) speed and torque.

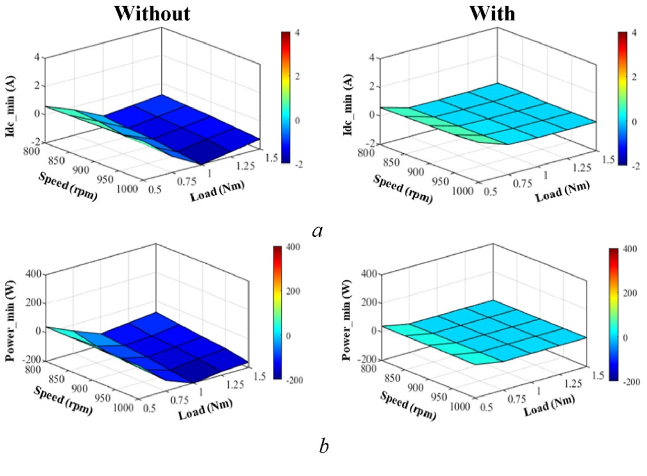

FIGURE 21 | Comparison of energy backflow issues without and with the proposed optimised FW method. (a) Minimum value of dc-link current, (b) Minimum value of inverter power.

energy backflow phenomenon in the transition is effectively reduced, and the fluctuations in dc-link current, power and torque are reduced. The system operates more stably, with much lower harmonic distortion in the dc-link current and torque. These measured results demonstrate the effectiveness of the proposed method in mitigating the energy backflow and improving the dynamic performance during speed ramp-up.

Figure 26 shows the results when the load increases from 0.2 Nm to 1.5 Nm at a constant speed of 600 rpm. In the left column, without employing the proposed method, the system exhibits instability due to the large dc-link voltage fluctuations. This causes the energy backflow phenomenon, leading to significant distortions in the dc-link current, power and torque, which further destabilise the system. In the right column, when the proposed method is used, the energy backflow phenomenon is eliminated. The harmonics in dc-link voltage, dc-link current and torque are greatly reduced. These results highlight the effectiveness of the proposed method in enhancing the dynamic control performance of the small dc-link capacitor-based PMSM drive system under varying load conditions.

In conclusion, Figures 25 and 26 validate that the proposed method improves the dynamic performance of the PMSM drive system by effectively eliminating energy backflow, reducing current and power harmonics, and stabilising system operation under both speed ramp-up and varying load conditions.

5 | Conclusion

This paper systematically identifies and analyses the energy backflow phenomenon in small dc-link capacitor-based IPMSM drive systems—an issue overlooked in existing research studies. This study demonstrates how energy backflow degrades system

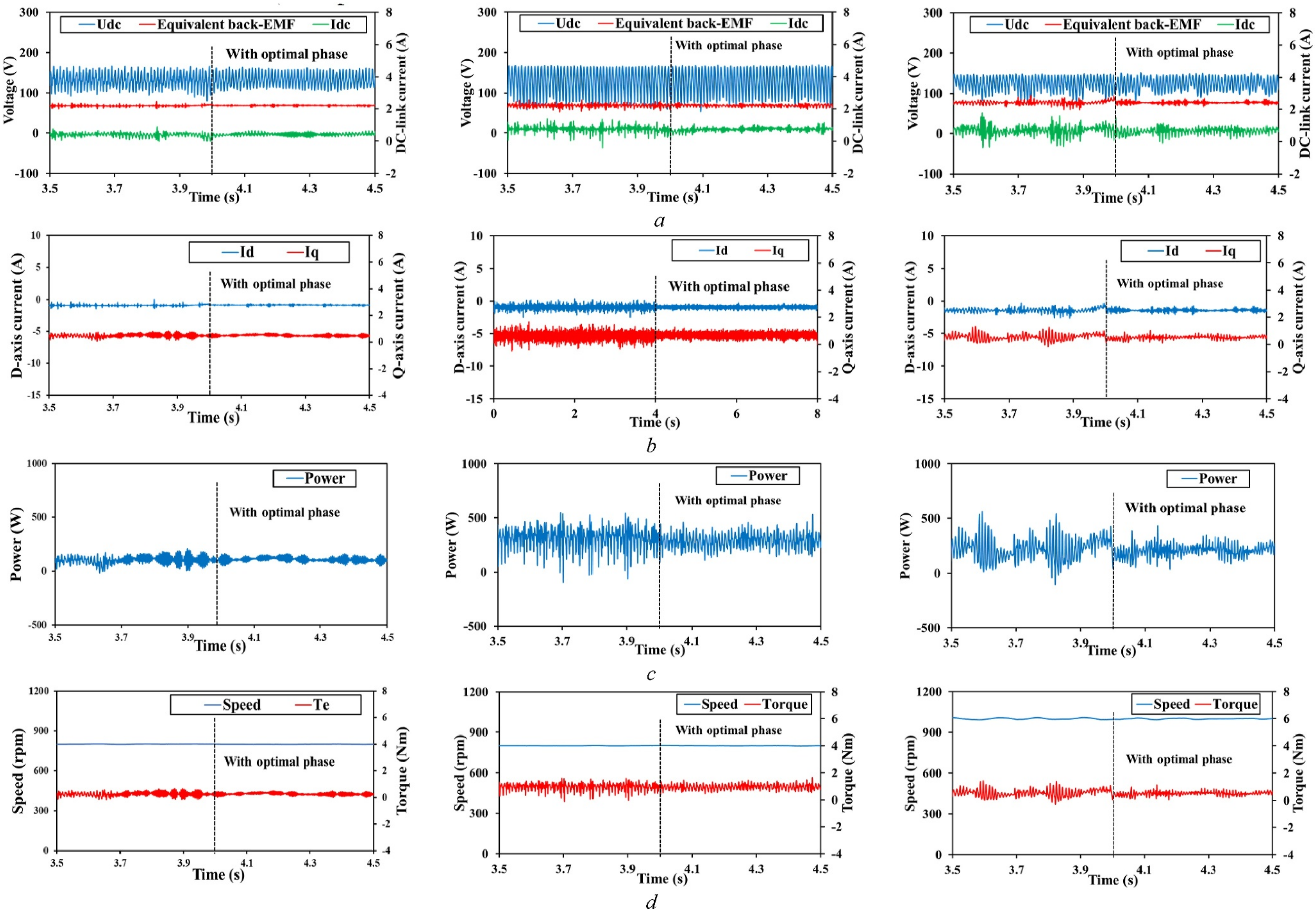

FIGURE 22 | Measured results without and with the proposed optimal phase angle selection method (from left to right, 800 rpm with 0.5 Nm load, 800 rpm with 1 Nm load, 1000 rpm with 0.5 Nm load). (a) DC-link voltage, equivalent back-EMF, and dc-link current, (b) dq-axis current, (c) Power, (d) Speed and torque.

TABLE 2 | Comparison of simulation and experimental results for the amplitude of the 100 Hz harmonic in the conventional FW method under DC-Link voltage fluctuations.

	Simulation				Experimental			
	DC-link voltage	D-axis current	Q-axis current	Power	DC-link voltage	D-axis current	Q-axis current	Power
800 rpm & 0.5 Nm	35 V	0.12 A	0.18 A	35 W	48 V	0.31 A	0.37 A	45 W
800 rpm & 1 Nm	51 V	0.36 A	0.42 A	54 W	65 V	0.48 A	0.53 A	82 W
1000 rpm & 0.5 Nm	42 V	0.18 A	0.31 A	41 W	59 V	0.37 A	0.45 A	61 W

TABLE 3 | Comparison of simulation and experimental results for the amplitude of the 100 Hz harmonic in the proposed methods under DC-Link voltage fluctuations.

	Simulation				Experimental			
	DC-link voltage	D-axis current	Q-axis current	Power	DC-link voltage	D-axis current	Q-axis current	Power
800 rpm & 0.5 Nm	18 V	0.05 A	0.09 A	20 W	22 V	0.1 A	0.12 A	25 W
800 rpm & 1 Nm	28 V	0.24 A	0.28 A	36 W	35 V	0.28 A	0.3 A	58 W
1000 rpm & 0.5 Nm	22 V	0.09 A	0.11 A	25 W	28 V	0.15 A	0.15 A	31 W

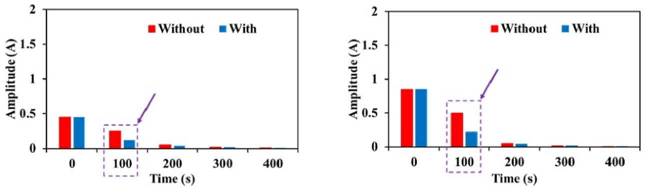

a *b*

FIGURE 23 | Spectra of q-axis current without and with proposed optimal phase angle selection method under different load. (a) 0.5 Nm, (b) 1 Nm.

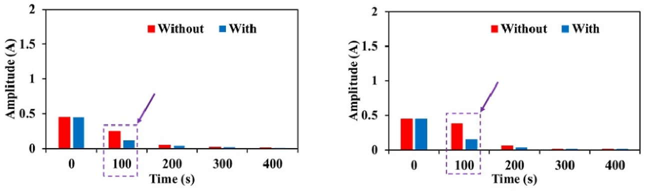

a *b*

FIGURE 24 | Spectra of q-axis current without and with proposed optimal phase angle selection method under different speed. (a) 800 rpm, (b) 1000 rpm.

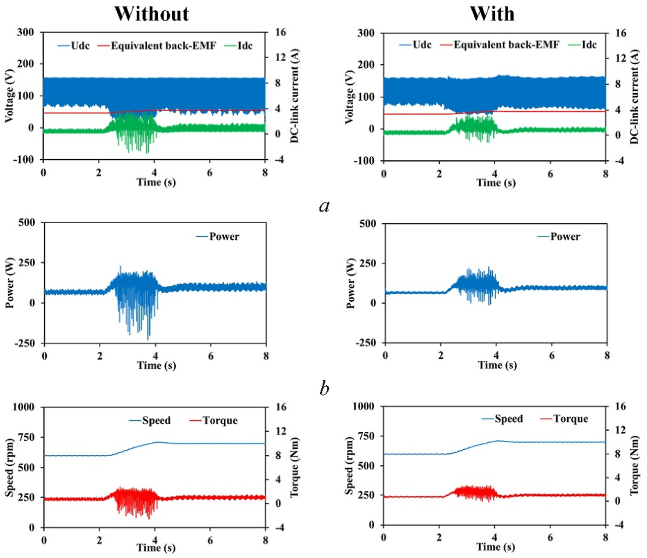

FIGURE 25 | Measured results with speed increased from 600 to 700 rpm without and with the proposed method. (a) DC-link voltage, equivalent back-EMF, and dc-link current, (b) Power, (c) Speed and torque.

performance, particularly during high-speed and/or high-load operations with severe dc-link voltage fluctuations. Furthermore, the limitations of conventional feedback FW control strategies under fluctuating dc-link voltage conditions are revealed, showing their potential to induce instability and degrade performance.

To address these challenges, a novel quasi-PIR-based FW control method with dc offset compensation is proposed to mitigate energy backflow. Additionally, a GD algorithm-based optimal phase angle selection strategy is introduced to suppress q-axis current harmonics and improve system control precision and stability.

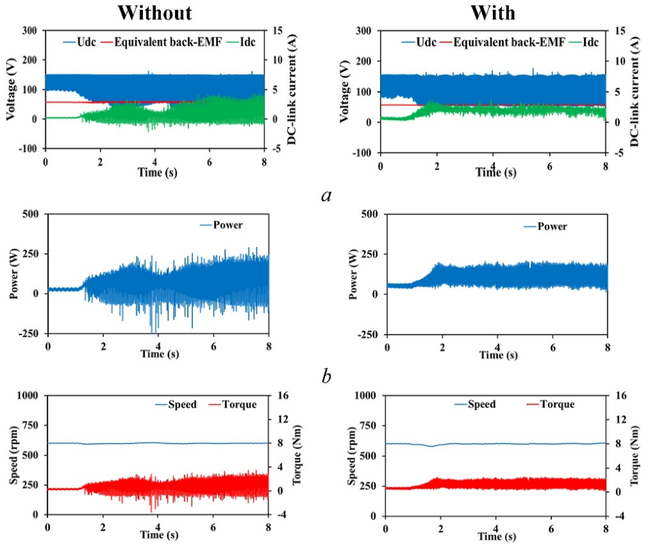

FIGURE 26 | Measured results with load increased from 0.2 Nm to 1.5 Nm without and with the proposed method. (a) DC-link voltage, equivalent back-EMF, and dc-link current, (b) Power, (c) Speed and torque.

Experimental validation confirms the theoretical analysis of the energy backflow phenomenon and demonstrates the effectiveness of the proposed methods. The results show significant improvements in system performance, including the elimination of energy backflow, suppression of current harmonics, and enhancement of control stability. These contributions provide a valuable foundation for advancing the design and operation of small dc-link capacitor-based IPMSM drive systems, particularly in industrial and high-performance applications where compact, efficient and reliable solutions are increasingly demanded.

Author Contributions

Jun Yan: investigation, methodology, validation, writing – original draft. **Zi Qiang Zhu:** methodology, project administration, writing – review and editing. **Ximeng Wu:** writing – review and editing. **Han Yang:** resources. **Lianghui Yang:** resources. **Chaohui Liu:** resources.

Conflicts of Interest

The Editor-in-Chief was not involved in the handling of the article or its peer review process. The Deputy Editor-in-Chief and handling Associate Editor have taken full responsibility of the editorial process for the article. There are no other conflicts of interest to disclose.

Data Availability Statement

Data available on request from the authors.

References

1. Z. Q. Zhu and D. Howe, "Electrical Machines and Drives for Electric, Hybrid, and Fuel Cell Vehicles," *Proceedings of the IEEE* 95, no. 4 (2007): 746–765, https://doi.org/10.1109/jproc.2006.892482.

2. T. M. Jahns and V. Caliskan, "Uncontrolled Generator Operation of Interior PM Synchronous Machines Following High-Speed Inverter

Shutdown," *IEEE Transactions on Industry Applications* 35, no. 6 (1999): 1347–1357, https://doi.org/10.1109/28.806049.

3. M. S. Huang and C. M. Liaw, "Speed Control for Field-Weakened Induction Motor Drive," *IEE Proceedings – Electric Power Applications* 152, no. 3 (2005): 565–576, https://doi.org/10.1049/ip-epa:20055168.

4. C. Gong, Y. Hu, C. Gan, G. Chen, and M. Alkahtani, "Modeling, Analysis, and Attenuation of Uncontrolled Generation for IPMSM-Based Electric Vehicles in Emergency," *IEEE Transactions on Industrial Electronics* 67, no. 6 (2020): 4453–4462, https://doi.org/10.1109/tie.2019.2926049.

5. Y. Xu, Y. Huang, B. Zheng, W. Zhang, Y. Li, and J. Zou, "Over-Current Protection Method for PMSM VSI With Small Dc-Link Capacitor," *IET Power Electronics* 11, no. 7 (2018): 1231–1238, https://doi.org/10.1049/iet-pel.2017.0668.

6. G. Wang, N. Zhao, G. Zhang, and D. Xu, *Reduced Dc-Link Capacitance AC Motor Drives* (Springer Nature, 2020).

7. H. Li, Q. Yin, Q. Wang, H. Luo, and Y. Hou, "A Novel Dc-Link Voltage Feedback Active Damping Control Method for IPMSM Drives With Small Dc-Link Capacitors," *IEEE Transactions on Industrial Electronics* 69, no. 3 (2022): 2426–2436, https://doi.org/10.1109/tie.2021.3066942.

8. D. Wang, K. Lu, P. O. Rasmussen, L. Mathe, Y. Feng, and F. Blaabjerg, "Voltage Modulation Using Virtual Positive Impedance Concept for Active Damping of Small DC-Link Drive System," *IEEE Transactions on Power Electronics* 33, no. 12 (2018): 10611–10621, https://doi.org/10.1109/tpel.2018.2799988.

9. L. Mathe, L. Török, D. Wang, and D. Sera, "Resonance Reduction for AC Drives With Small Capacitance in the DC Link," *IEEE Transactions on Industry Applications* 53, no. 4 (2017): 3814–3820.

10. Z. Ren, D. Ding, G. Wang, et al., "Adaptive Virtual Admittance Reshaping-Based Resonance Suppression Strategy for PMSM Drives With Small DC-Link Capacitor," *IEEE Transactions on Power Electronics* 39, no. 3 (2024): 3109–3121, https://doi.org/10.1109/tpel.2023.3341901.

11. H. S. Jung, S. J. Chee, S. K. Sul, Y. J. Park, H. S. Park, and W. K. Kim, "Control of Three-Phase Inverter for Ac Motor Drive With Small DC-Link Capacitor Fed by Single-Phase AC Source," *IEEE Transactions on Industry Applications* 50, no. 2 (2014): 1074–1081, https://doi.org/10.1109/tia.2013.2288238.

12. Q. Yin, H. Li, H. Luo, Q. Wang, J. Miao, and Y. Hou, "Grid Input Current Feedback Active Damping Control Method for IPMSM Drives With Small DC-link Capacitor," *IET Power Electronics* 14, no. 3 (2021): 640–650, https://doi.org/10.1049/pel2.12052.

13. R. Maheshwari, S. Munk-Nielsen, and K. Lu, "An Active Damping Technique for Small DC-Link Capacitor Based Drive System," *IEEE Transactions on Industrial Informatics* 9, no. 2 (2013): 848–858, https://doi.org/10.1109/tii.2012.2222036.

14. W. J. Lee and S. K. Sul, "DC-Link Voltage Stabilization for Reduced Dc-Link Capacitor Inverter," *IEEE Transactions on Industry Applications* 50, no. 1 (2014): 404–414.

15. N. Zhao, G. Wang, D. Xu, L. Zhu, G. Zhang, and J. Huo, "Inverter Power Control Based on Dc-Link Voltage Regulation for IPMSM Drives Without Electrolytic Capacitors," *IEEE Transactions on Power Electronics* 33, no. 1 (2018): 558–571, https://doi.org/10.1109/tpel.2017.2670623.

16. I. Takahashi and H. Haga, "Power Factor Improvement of Single-phase Diode Rectifier by Fast Field-Weakening of Inverter Driven IPM Motor," *IEEE 4th Int. Conf. Power Electron. Drive Syst.* 2, no. 1 (2001): 241–246.

17. Y. Son and J. I. Ha, "Direct Power Control of a Three-Phase Inverter for Grid Input Current Shaping of a Single-Phase Diode Rectifier With a Small DC-Link Capacitor," *IEEE Transactions on Power Electronics* 30, no. 7 (2015): 3794–3803, https://doi.org/10.1109/tpel.2014.2345421.

18. Y. Son and J. I. Ha, "Discontinuous Grid Current Control of Motor Drive System With Single-phase Diode Rectifier and Small DC-Link Capacitor," *IEEE Transactions on Power Electronics* 32, no. 2 (2017): 1324–1334, https://doi.org/10.1109/tpel.2016.2544400.

19. K. Abe, H. Haga, K. Ohishi, and Y. Yokokura, "Fine Current Harmonics Reduction Method for Electrolytic Capacitor-Less and Inductor-Less Inverter Based on Motor Torque Control and Fast Voltage Feedforward Control for IPMSM," *IEEE Transactions on Industrial Electronics* 64, no. 2 (2017): 1071–1080, https://doi.org/10.1109/tie.2016.2614270.

20. K. Abe, H. Haga, K. Ohishi, and Y. Yokokura, "Direct DC-Link Current Control Considering Voltage Saturation for Realization of Sinusoidal Source Current Waveform Without Passive Components for IPMSM Drives," *IEEE Transactions on Industrial Electronics* 65, no. 5 (2018): 3805–3814, https://doi.org/10.1109/tie.2017.2760289.

21. N. Zhao, G. Wang, R. Zhang, B. Li, Y. Bai, and D. Xu, "Inductor Current Feedback Active Damping Method for Reduced DC-link Capacitance IPMSM Drives," *IEEE Transactions on Power Electronics* 34, no. 5 (2019): 4558–4568, https://doi.org/10.1109/tpel.2018.2864247.

22. P. Magne, D. Marx, B. Nahid-Mobarakeh, and S. Pierfederici, "Large-signal Stabilization of a DC-Link Supplying a Constant Power Load Using a Virtual Capacitor: Impact on the Domain of Attraction," *IEEE Transactions on Industry Applications* 48, no. 3 (2012): 878–887, https://doi.org/10.1109/tia.2012.2191250.

23. K. Li, T. Sun, H. Li, Y. Wang, W. Li, and L. Gong, "Grid Current Quality Improvement for Three-phase Diode Rectifier-Fed Small DC-Link Capacitance IPMSM Drives," *IEEE Transactions on Energy Conversion* 37, no. 4 (2022): 2310–2320, https://doi.org/10.1109/tec.2022.3176143.

24. S. Taghizadeh, M. K. Ghartemani, M. J. Hossain, and J. Lu, "A Fast and Robust DC-Bus Voltage Control Method for Single-phase Voltage-Source DC/AC Converters," *IEEE Transactions on Power Electronics* 34, no. 9 (2019): 9202–9212, https://doi.org/10.1109/tpel.2018.2883464.

25. Y. Huang, Y. Xu, Y. Li, and J. Zou, "A Modified Sensorless Method for PMSM Drive With Small Dc-Link Capacitor," in *2017 IEEE Trans. Electrif. Conf. Expo, Asia-Pacific*, 2017), 1–5.

26. J. Huo, N. Zhao, R. Gao, G. Zhang, G. Wang, and D. Xu, "Analysis and Compensation of Position Estimation Error for Sensorless Reduced Dc-Link Capacitance IPMSM Drives," *IEEE Transactions on Industrial Electronics* 70, no. 3 (2023): 3213–3221, https://doi.org/10.1109/tie.2022.3170637.

27. W. Ding, L. Huo, and S. Chen, "A Novel Suppression Method for Position Estimation Error in Sensorless Control of Electrolytic Capacitor-Less PMSM Drives," *IEEE Journal of Emerging and Selected Topics in Power Electronics* 12, no. 1 (2024): 618–630, https://doi.org/10.1109/jestpe.2023.3342629.

28. A. Rabiei, T. Thiringer, M. Alatalo, and E. A. Grunditz, "Improved Maximum-Torque-Per-Ampere Algorithm Accounting for Core Saturation, Cross-Coupling Effect, and Temperature for a PMSM Intended for Vehicular Applications," *IEEE Transactions on Transportation Electrification* 2, no. 2 (2016): 150–159, https://doi.org/10.1109/tte.2016.2528505.

29. J. Yan, X. Wu, Z. Q. Zhu, and C. Liu, "Improved Extended EMF-Based Sensorless Control for IPMSMs With Small DC-Link Capacitor Considering DC-Link Voltage Measurement Error," *IEEE Transactions on Industry Applications* 60, no. 4 (2024): 6299–6313, https://doi.org/10.1109/tia.2024.3397960.

30. W. J. Lee, S. K. Sul, and Y. S. Shim, "A Protection Scheme Against Voltage Sags for Electrolytic Capacitorless AC Drives," *IEEE Transactions on Industry Applications* 45, no. 1 (2009): 186–193, https://doi.org/10.1109/tia.2008.2009497.

31. D. Ding, G. Wang, N. Zhao, G. Zhang, and D. Xu, "Enhanced Flux-Weakening Control Method for Reduced DC-Link Capacitance IPMSM

Drives," *IEEE Transactions on Power Electronics* 34, no. 8 (2019): 7788–7799, https://doi.org/10.1109/tpel.2018.2878877.

32. J. Huo, D. Ding, Z. Ren, et al., "A Novel Flux-Weakening Control Method With Quadrature Voltage Constraint for Electrolytic Capacitorless PMSM Drives," *CES Transactions on Electrical and Machines System* 6, no. 3 (2022): 279–287, https://doi.org/10.30941/cestems.2022.00038.

33. R. Jing, D. Ding, G. Zhang, et al., "Active-Damping-Based Field-Weakening Control Strategy With Voltage Angle Regulation for High-Speed SPMSM Drive," *IEEE Transactions on Industrial Electronics* 71, no. 2 (2024): 1421–1431, https://doi.org/10.1109/tie.2023.3262850.

34. J. Jacob, O. Bottesi, S. Calligaro, and R. Petrella, "Design Criteria for Flux-Weakening Control Bandwidth and Voltage Margin in IPMSM Drives Considering Transient Conditions," *IEEE Transactions on Industry Applications* 57, no. 5 (2021): 4884–4900, https://doi.org/10.1109/tia.2021.3085535.

35. Q. Hou, H. Wang, C. Zhao, et al., "Super-Twisting Extended State Observer-Based Quasi-Proportional-Resonant Controller for Permanent Magnet Synchronous Motor Drive System," *IEEE Transactions on Transportation Electrification* 10, no. 1 (2024): 1596–1604, https://doi.org/10.1109/tte.2023.3285761.

36. C. Lai, G. Feng, J. Tian, et al., "PMSM Drive System Efficiency Optimization Using a Modified Gradient Descent Algorithm With Discretized Search Space," *IEEE Transactions on Transportation Electrification* 6, no. 3 (2020): 1104–1114, https://doi.org/10.1109/tte.2020.3004463.